energies

MDPI

Article

Numerical Investigation on the Effect of Passive Jet Control on the Performance of a Vortex Induced Vibration Energy Harvester System

Dineshkumar Ravi [1], Grzegorz Litak [1,*], Mateusz Waśkowicz [1] and Marcin Fronc [2]

[1] Faculty of Mechanical Engineering, Lublin University of Technology, 20-618 Lublin, Poland; d.ravi@pollub.pl (D.R.); mateusz.waskowicz1@pollub.edu.pl (M.W.)
[2] Faculty of Electrical Engineering, Lublin University of Technology, 20-618 Lublin, Poland; m.fronc@pollub.pl
* Correspondence: g.litak@pollub.pl

Abstract: The present study investigates the effect of the passive jet control system on the performance of a vibration energy harvester system (VIVEHS). The shape of a bluff body plays a crucial role in determining the vortex shedding mechanism, while the passive jet control system influences the dynamic behavior of these vortices, either enhancing or suppressing the bluff body's oscillatory performance. This study introduces key innovations, including the incorporation of perforations in the bluff body, variations in outlet angles, and different inlet and outlet configurations. In this regard, a two-dimensional numerical investigation has been carried out to understand and optimize the dynamic response from the bluff body and its effect on beam deflection. The validation of the numerical code has been carried out for a cylindrical shaped bluff body using ANSYS Fluent 23.2 numerical modelling software. Upon validation, the effects of a single inlet and a symmetrical dual outlet with different outlet angles are numerically analyzed under various flow conditions to assess their impact on the dynamic behavior of the system. The outlet angle varies between 30 degrees and 120 degrees with intervals of 30 degrees. The contours of vorticity and the bluff body dynamic characteristics were observed and plotted for various flow conditions ranging between 1 m/s and 8 m/s with intervals of 1 m/s. The results of this numerical study are crucial for designing passive jet control systems in practical energy harvesting applications. The optimization of outlet configurations and control strategies can significantly enhance both the efficiency and stability of energy harvesting systems.

Keywords: vortex induced vibration; energy harvester; passive jet control system; computational fluid dynamics; numerical simulation

Academic Editor: Philippe Leclère

Received: 26 December 2024
Revised: 3 February 2025
Accepted: 6 February 2025
Published: 8 February 2025

Citation: Ravi, D.; Litak, G.; Waśkowicz, M.; Fronc, M. Numerical Investigation on the Effect of Passive Jet Control on the Performance of a Vortex Induced Vibration Energy Harvester System. *Energies* **2025**, *18*, 793. https://doi.org/10.3390/en18040793

1. Introduction

Vortex-Induced Vibration Energy Harvester Systems (VIVEHS) have gained significant attention over the past decade due to their substantial impact on addressing power supply challenges in remote areas with limited access to power grids. Operating small equipment and various wireless sensors for applications such as environmental monitoring, agricultural data collection, and security systems often incurs high costs when relying on conventional power sources [1]. Although various energy-harvesting technologies like wind- and solar-based harvesters are available, they are associated with high operating costs and maintenance requirements. In contrast, Vortex-Induced Vibration Energy Harvester Systems (VIVEHS) efficiently convert structural vibrations into useful energy, offering a more cost-effective and low-maintenance solution [2,3]. As fluid flows around a bluff body with a circular cross-section, the adverse pressure gradient downstream of the body causes the boundary layer to separate from the bluff body surface. This flow separation results in the formation of vortices, which are shed alternately from opposite sides of the body, commonly known as vortex shedding [4,5]. The frequency of vortex shedding is greatly influenced by several factors, including the Reynolds number of the incoming flow, as well as geometric characteristics such as the size and shape of the bluff body [6]. The relationship between the inlet Reynolds number, the dimensions of the bluff body, and the vortex shedding frequency is expressed by the Strouhal number [7]. When the natural frequency of the bluff body coincides with the vortex shedding frequency, the system undergoes resonance and yields maximum oscillation amplitude. This synchronization zone where the amplitude of the bluff body oscillations reaches its maximum, known as the frequency lock-in region, is characterized by strong coupling between fluid dynamics and structural vibrations [8]. Owen et al. [9] carried out an experimental investigation on three configurations, namely a conventional circular cylinder, a circular cross-sectional body with a sinuous axis, and a circular cylinder with hemispherical bumps. They predicted that the introduction of a sinuous axis in the circular cylinder led to a significant suppression of vortex shedding and drag characteristics by 47%, and for the cylinder with hemispherical bumps by 25%, respectively. Additionally, they observed that the mass damping required to stabilize the cylinder with a sinuous axis or hemispherical bumps was lower than that required for a conventional circular cylinder. Chen et al. [10] investigated the effectiveness of passive jet control in suppressing the vibrations of a circular cylinder. The test system consists of a conventional circular cylinder and a jet pipe with multiple inlets and outlets, configured with four different spacing ratios, namely 0.38, 1.15, 2.69 and 3.46. Their findings demonstrated that the introduction of passive jets effectively suppressed vortex formation and altered the dynamic characteristics of the system without requiring external energy. They further concluded that the optimal spacing of 0.38D at a reduced velocity (Vr) of 5.93 resulted in a maximum suppression of VIV by 99.52%. They also developed and analyzed a coupled model to study the VIV dynamics of a conventional circular cylinder and a cylinder equipped with a passive jet control system, providing deeper insights into the mechanisms underlying vibration suppression [11]. Chen et al. [12] investigated an experimental and coupled model of an active jet suppressing the VIV of a box girder. They revealed that the box girder equipped with the active jet system suppressed vibration amplitude more than the configurations without the active jet system. They suggested that the active jet control system technique would mitigate the VIV in box girders, enhancing its durability and safety. Youssef et al. [13] carried out an experimental investigation on passive control methods to suppress VIV in circular cylinders with low mass ratios, which were free to oscillate in both streamwise and transverse directions (two degrees of freedom). Their simplified experiments, performed in a rotating water tank, demonstrated that fin plates effectively reduced VIV by 80% by altering the flow patterns around the cylinder, thereby decreasing vibration amplitudes. They concluded that the optimized fin plate configurations were particularly effective in reducing resonant vibrations at natural frequencies. Wang et al. [14] carried out experimental and numerical investigations to evaluate the impact of an energy concentration pipe (ECP) with a passive jet control system on the performance of a VIV energy harvester. Their study considered ECP configurations with a single outlet, symmetrical dual outlets, and asymmetrical dual outlets with varying outlet angles. They found that the symmetrical dual outlet with an outlet angle of 60 degrees significantly widened the lock-in region by 108% and increased the maximum output voltage by 12.68% compared to the baseline case. Furthermore, they demonstrated that manipulating vortex shedding and controlling the delay or advancement of flow separation effectively amplified vibrations, thereby enhancing the energy harvesting efficiency. Wu et al. [15] investigated the CFD-DEM techniques with a varying viscosity profile to study the shear thickening polishing process and focused on the impact of microbubbles on abrasive particle behavior and grinding efficiency. Their approach includes a three-stage shear thickening model validated in bubble rise experiments. This could be beneficial in the present study for understanding the effects of viscosity on lift and drag characteristics and could help to more accurately predict the dynamic behavior of fluids in energy harvesting systems. Wang et al. [16] proposed a fluid–structure interaction (FSI) approach using a penalty function method for thin shells with liquid-filled interlayers and a constitutive relation based on the Voce equation for plastic hardening. The study employs an arbitrary Lagrange–Euler (ALE) method with the partial absolute nodal coordinate formulation (ANCF) to analyze the dynamic evolution and large deformations of RRC shells under various impact conditions. This approach can be useful in the present study for understanding the dynamic response of structures under large deformations and improving modeling techniques for tracking transient behavior during impact events. Wu et al. [17] conducted a numerical investigation on the impact of synthetic jet control on the energy harvesting performance of a semi-active flapping airfoil. Their investigation considered a two-dimensional elliptical airfoil shape, maintaining an inlet Reynolds number of 1100 throughout the study. The results indicated that incorporating synthetic jets enhanced efficiency from 16.9% to 31.6% compared to a system without synthetic jets. Additionally, they confirmed that the use of synthetic jets significantly increased the lift force, making it a promising approach for improving energy harvesting efficiency. Guo et al. [18] conducted a two-dimensional numerical investigation on the effects of pulsed blowing jets on the VIV of a circular cylinder. The pulsed blowing jets were positioned perpendicular to the flow direction and located on the upper surface of the cylinder. Their findings showed that at lower values of the coefficient of lift (Cl), the vortices remained trapped in the shear layer. As Cl increased, the vortices grew stronger, with smaller eddies merging into larger ones, leading to more complex vortex patterns and oscillation modes. At Cl values above 0.1, the oscillations intensified, sometimes resulting in galloping. The study concluded that vortex interactions are highly sensitive to Cl, with varying oscillation modes and power gain efficiency under different conditions.

Earlier studies on passive jet control systems demonstrated their significant role in vibration suppression across various mechanical structures. The passive suction and jetting of flow around a bluff body strongly influence the vortex shedding mechanism, thereby altering the wake formation behind the body. These passive jet control systems are primarily utilized to control and suppress vibrations in mechanical structures. However, relatively few studies have explored the effectiveness of passive jet systems in the context of energy harvesting. The present study investigates the effect of passive jet control systems in regulating the frequency and transverse oscillations of a bluff body under varying inlet Reynolds numbers. The novelty of the present study is the incorporation of perforated holes in the bluff body, enabling a single inlet with multiple outlet configurations to enhance flow separation and energy dissipation. Initially, a two-dimensional numerical analysis is performed to examine the effects of symmetrical dual outlets with varying outlet angles under diverse flow conditions. The key innovation lies in the single-inlet, multiple-outlet design, which provides greater flexibility in controlling oscillatory behavior while reducing the complexity of traditional active control systems. The results would offer insights into optimizing passive jet designs for improved aerodynamic stability and flow control. This approach addresses the limitations of existing methods by presenting an energy-efficient, passive solution for enhancing flow stability and system performance.

2. Numerical Methodology

A two-dimensional numerical investigation of the passive jet control system consists of three phases, namely preprocessing, processing and post processing. In the preprocessing phase, the numerical model of a bluff body and enclosure have been modelled using SolidWorks 2019 modelling software. The base model of a bluff body is maintained as a circular profile. The base model is then perforated with a single inlet and a symmetrical dual outlet with various outlet angles. The baseline configuration consists of a circular cross-sectional profile, while the modified cases incorporate holes/perforations with a single inlet and symmetrical dual outlets at varying outlet angles, namely 30°, 60°, 90°, and 120°. The incoming wind velocities are varied between 1 m/s and 8 m/s with intervals of 1 m/s to understand the dynamic behavior of the passive jet system with various inflow conditions, as shown in Figure 1. The thicknesses of the inlet and outlet channels were maintained as 5 mm and the length and diameter of the bluff body were maintained as 100 mm and 60 mm respectively. The dimensions of the enclosure were maintained as 25D × 33D. The two-dimensional numerical model of a bluff body with the enclosure were discretized into nearly 4.6 million hexahedral elements through the finite volume approach using ANSYS ICEMCFD 23.2, as shown in Figure 2, and the mesh model is then imported to ANSYS Fluent 23.2 solver to apply the required boundary conditions. In the processing phase, the fluid flow variations through and across the bluff body were captured by solving the governing equations, namely mass and momentum equations, and the Shear Stress Transport (SST) k-ω mode of closure was used to capture the turbulence. The convergence criterion was maintained as 10^{-6} and a monitor point was created for lift, drag and displacement characteristics. The numerical simulation was carried out for a total period of 10 s with a time step size of 0.001 s, and therefore a total number of 10,000 steps were considered for the study. The maximum number of iterations chosen for each step size is 30, and the convergence was achieved between 20 and 30 iterations for different geometrical and boundary conditions for the various numerical simulations considered in this study. In the last phase, the results of the present study, contours of vorticity, and oscillation amplitude were plotted and compared with the other models to determine the best suitable outlet angle against various flow conditions.

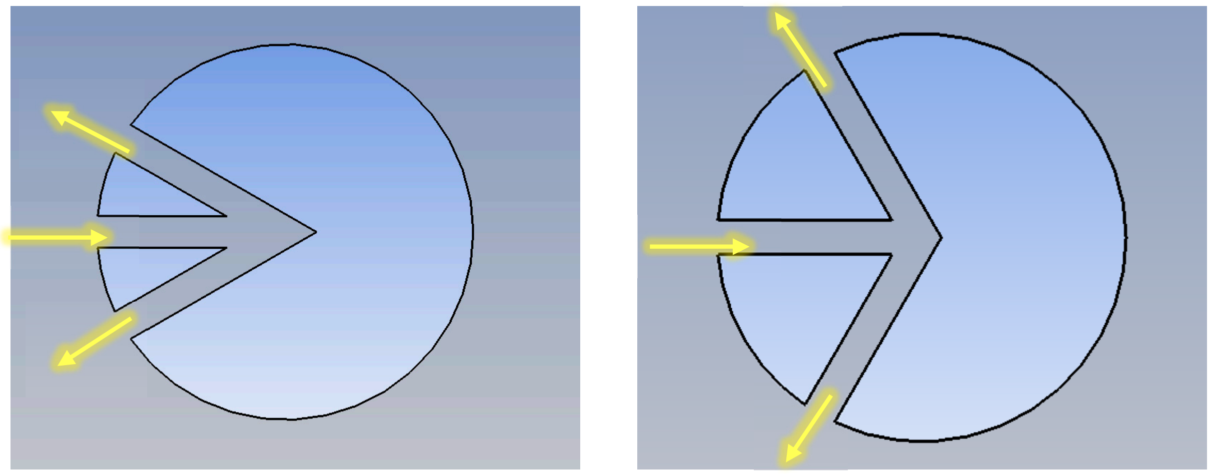

(**a**) (**b**)

Figure 1. *Cont.*

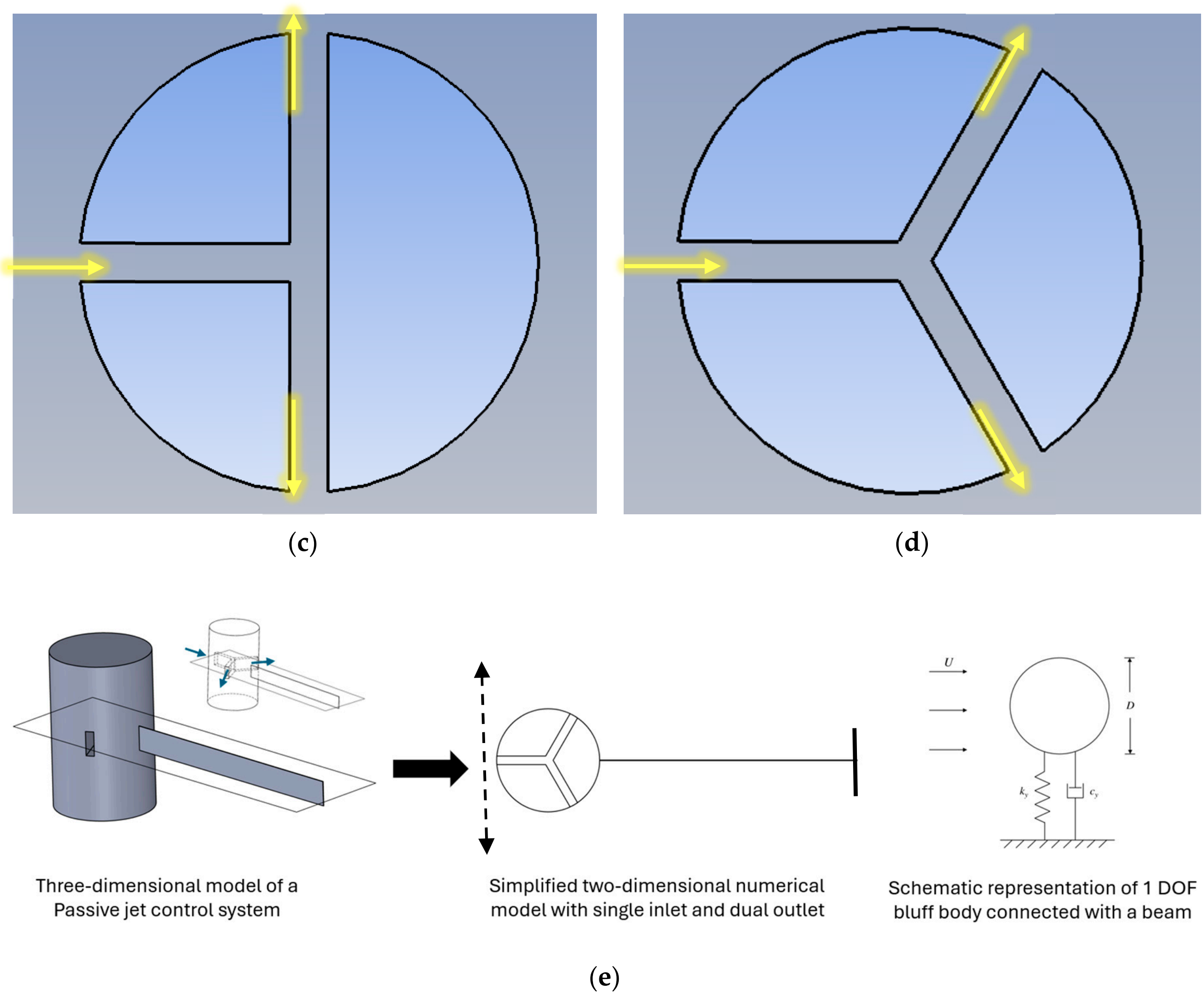

Figure 1. Numerical model of a bluff body with a single inlet and dual outlets (**a**) 30° (**b**) 60°, (**c**) 90°, (**d**) 120° and (**e**) schematic representation of the passive jet control system.

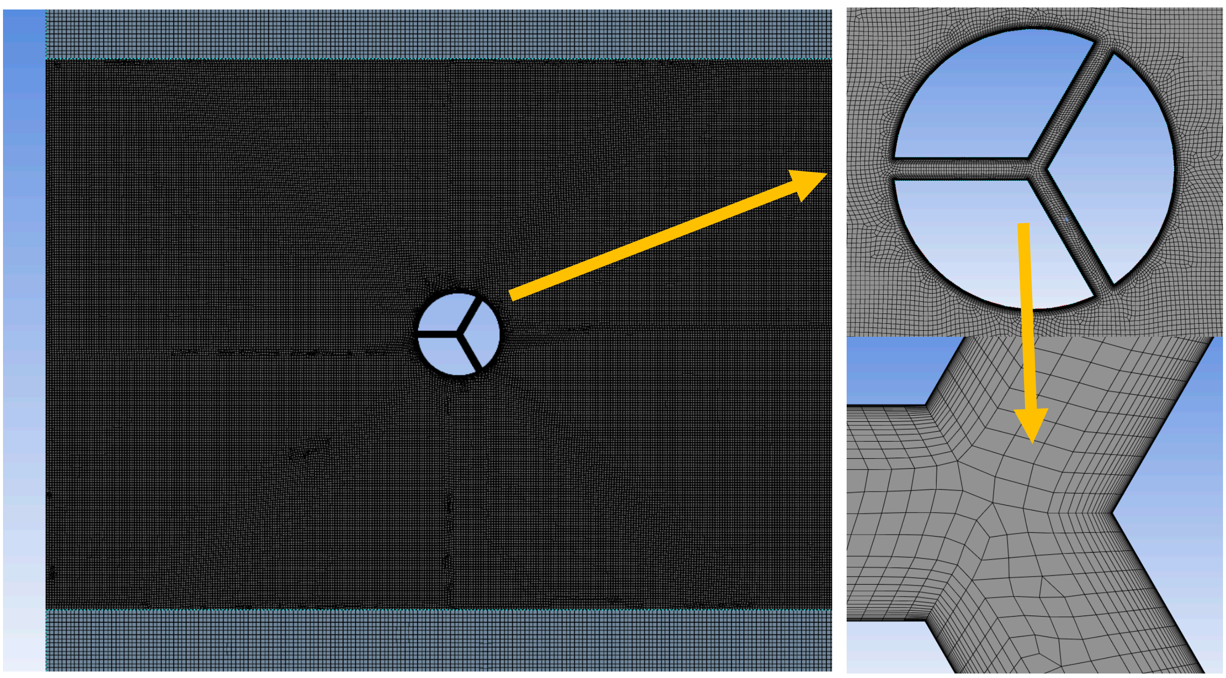

Figure 2. Discretized model of the bluff body and enclosure.

2.1. Grid Independence Study

The grid independence study, commonly known as the mesh sensitivity test, was carried out to ensure that the grid elements are independent of the predicted aerodynamic forces. In this study, the face sizing value was varied from 3 mm, 2 mm, 1 mm, and 0.5 mm for the inner domain and enclosure, and the corresponding grid elements are nearly 0.325 million, 0.375 million, 0.45 million, and 0.778 million, respectively. It was observed that when the grid elements increase from 0.325 to 0.45 million elements, the maximum oscillation amplitude tends to decrease from 43 mm to 37.8 mm, which corresponds to nearly 12% deviation, as shown in Figure 3. When the number of elements is increased beyond 0.45 million elements, there is no significant variation in the oscillation amplitude. Hence for the present study, the number of elements has been maintained above 0.45 million elements for all the numerical investigations.

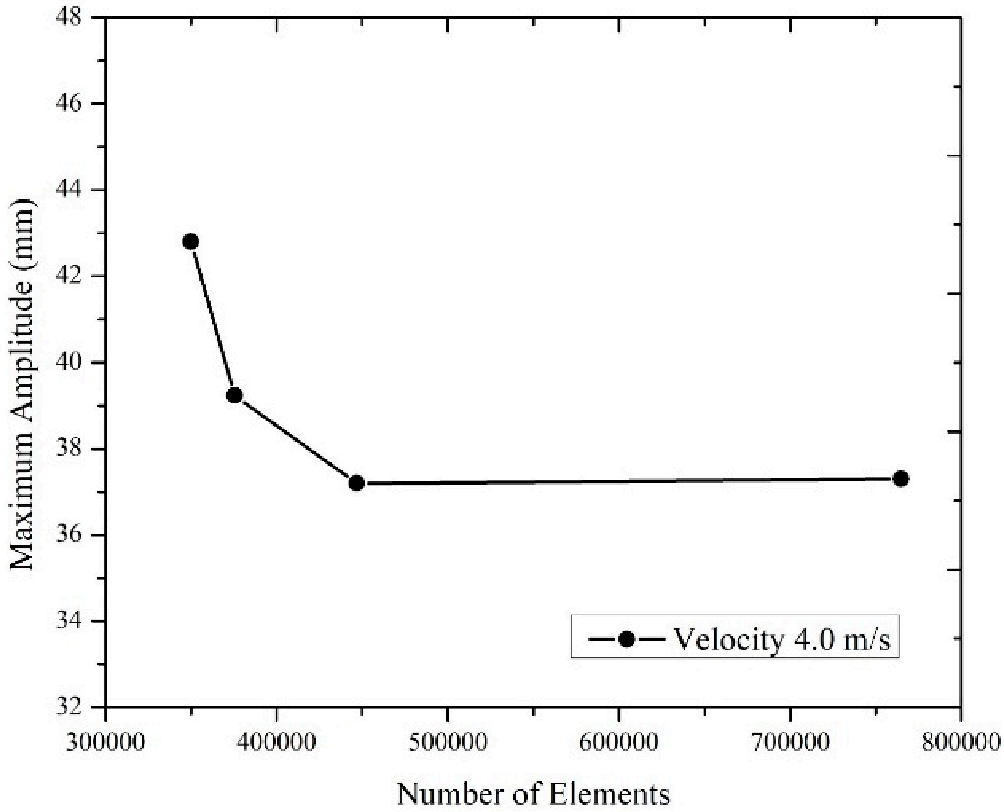

Figure 3. Grid independence study plot.

2.2. Time Independence Study

Similarly, a time independent study has also been carried out to optimize the time step size. The numerical study was extended to a total time of 10 s and a time stepping size of 0.1, 0.05, 0.02, and 0.01 was varied for an inlet velocity of 4 m/s. It was observed that when the time step size decreased from 0.1 to 0.02, the maximum oscillation amplitude also varied from 35 mm to 37.2 mm, which corresponds to 6.7% deviation, as shown in Figure 4. After decreasing the time step size, there is no noticeable difference in oscillation amplitude. Hence, for all the studies, the time step size value of 0.01 s has been maintained.

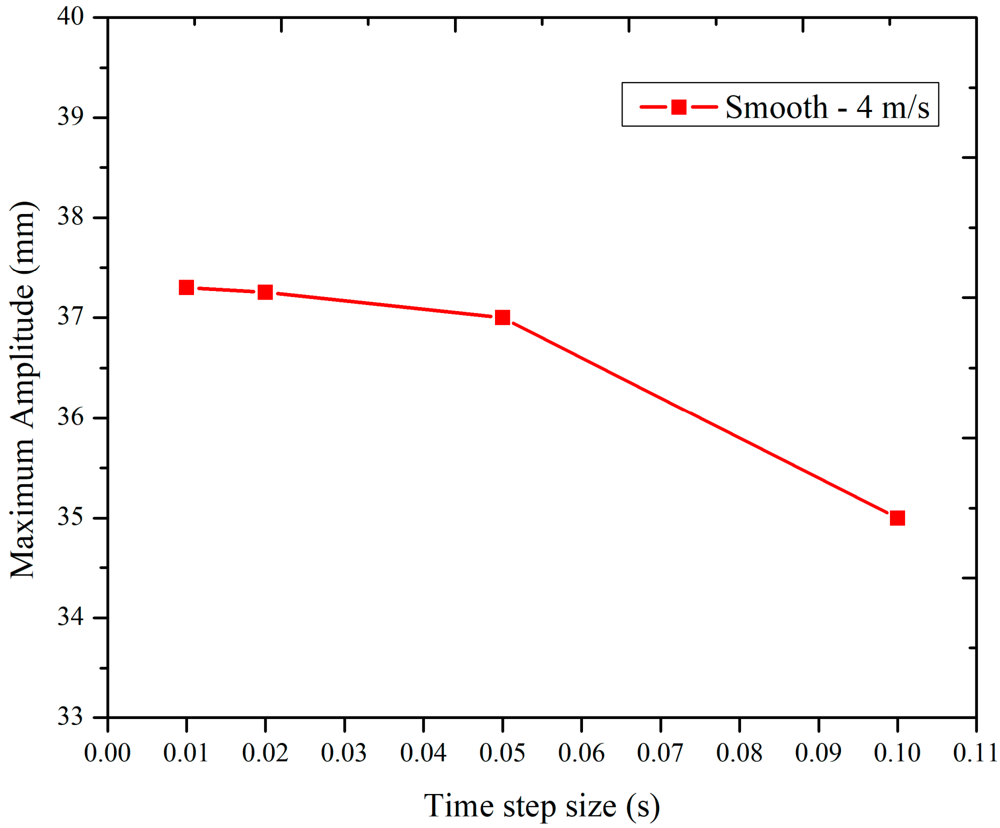

Figure 4. Time step independence study plot.

2.3. Assumptions & Boundary Conditions

The assumption involved in the present study is incompressible air. The nature of the problem is unsteady, focusing on the time-dependent behavior of vortex shedding and structural response. The bluff body is treated as a rigid body, simplifying the interaction between fluid and structure. The inlet velocity was maintained between 1 m/s and 8 m/s with intervals of 1 m/s. The top and bottom wall was treated as symmetrical, and therefore the wall effects will not influence the harvester system. An interface was created between the two fluid domains, inner and the enclosure. The interface option enables us to transfer all the flow properties, such as velocity and pressure, between the adjacent zones. The outlet boundary was maintained as atmospheric pressure as shown in Table 1. The numerical model of the bluff body is shown in Figure 5.

Table 1. Boundary conditions.

S. No	Boundary Name	Type	Values
1	Inlet—Outer, Inner domain	Velocity Inlet	1 m/s to 8 m/s
2	Top Wall	Symmetry	Symmetry
3	Bottom Wall	Symmetry	Symmetry
4	Outlet	Pressure Outlet	101,325 Pa (1 atm)
5	Inner domain—Top, bottom and back	Interface	Interface
6	Cylinder	Adiabatic wall	No slip

The fluid is assumed to be incompressible, unsteady/transient, and rigid body—bluff body.

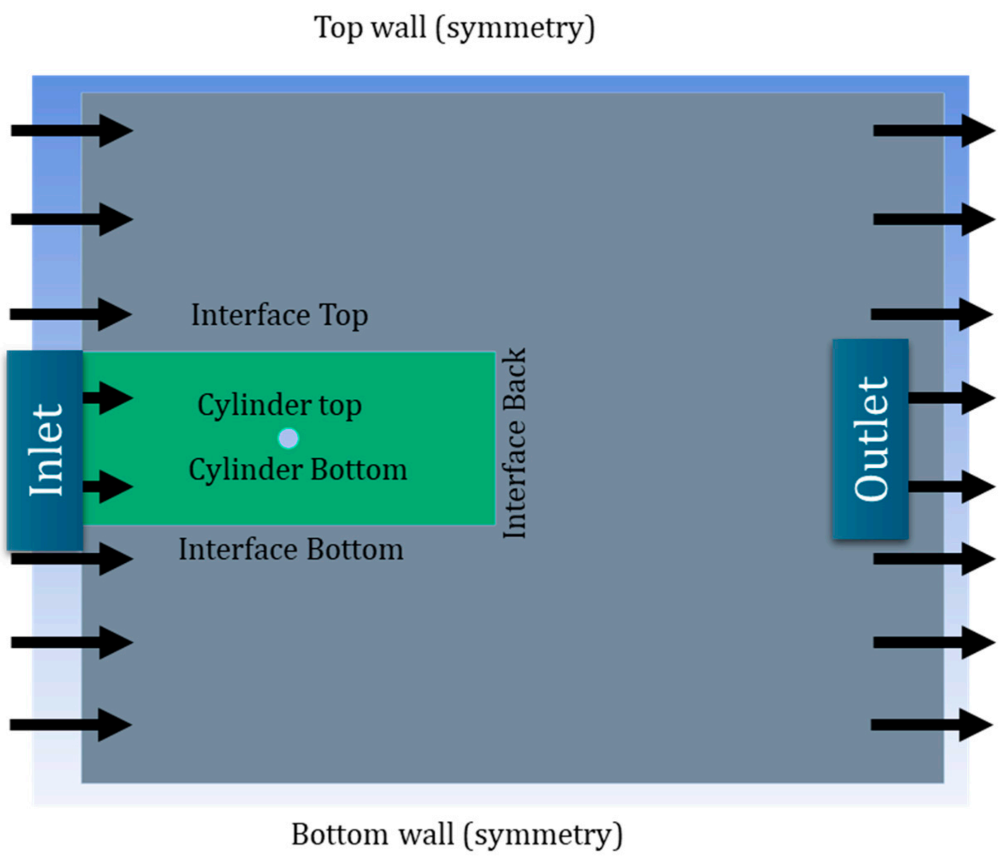

Figure 5. Numerical model of the bluff body with the enclosure.

2.4. Mathematical Modeling and Solution Techniques

A two-dimensional simplified model of a beam integrated with the bluff body was solved numerically through the finite volume approach using ANSYS Fluent 23.2 commercial CFD code. The fluid flow variations across various bluff body shapes were simulated by solving the governing equations, namely conservation of mass and momentum. The turbulence induced in the flow was captured by solving the Shear Stress Transport (SST) k-ω mode of closure.

2.4.1. Conservation of Mass

$$\frac{\partial u}{\partial x} + \frac{\partial v}{\partial y} = 0 \tag{1}$$

2.4.2. Conservation of Momentum

The scalar momentum equation of velocity component in the x direction is given by

$$\frac{\partial u}{\partial t} + u\frac{\partial u}{\partial x} + v\frac{\partial u}{\partial y} = -\frac{1}{\rho}\frac{\partial p}{\partial x} + \vartheta\left(\frac{\partial^2 u}{\partial x^2} + \frac{\partial^2 u}{\partial y^2}\right) - \frac{\partial \tau_{txx}}{\partial x} - \frac{\partial \tau_{txy}}{\partial y}. \tag{2}$$

The scalar momentum equation of the velocity component in the y direction is given by

$$\frac{\partial v}{\partial t} + u\frac{\partial v}{\partial x} + v\frac{\partial v}{\partial y} = -\frac{1}{\rho}\frac{\partial p}{\partial y} + \vartheta\left(\frac{\partial^2 v}{\partial x^2} + \frac{\partial^2 v}{\partial y^2}\right) - \frac{\partial \tau_{tyx}}{\partial x} - \frac{\partial \tau_{tyy}}{\partial y}, \tag{3}$$

where $\vartheta = \frac{\mu}{\rho}$.

2.4.3. Transport Equation for the k-ω Turbulence Model

The turbulent kinetic energy "k" of the standard k-ω two-equation model is given by

$$\frac{\partial k}{\partial t}+u\frac{\partial k}{\partial x}+v\frac{\partial k}{\partial y}=\frac{\partial}{\partial x}\left[\left(\vartheta+\sigma_{k\ \vartheta_t}\right)\frac{\partial k}{\partial x}\right]+\frac{\partial}{\partial y}\left[\left(\vartheta+\sigma_{k\ \vartheta_t}\right)\frac{\partial k}{\partial y}\right]+P_k-\beta\rho k\omega. \quad (4)$$

The turbulent dissipation rate "ω" of the standard k-ω two-equation model is given by

$$\frac{\partial \omega}{\partial t}+u\frac{\partial \omega}{\partial x}+v\frac{\partial \omega}{\partial y}=\frac{\partial}{\partial x}\left[\left(\vartheta+\sigma_{\omega\ \vartheta_t}\right)\frac{\partial \omega}{\partial x}\right]+\frac{\partial}{\partial y}\left[\left(\vartheta+\sigma_{\omega\ \vartheta_t}\right)\frac{\partial \omega}{\partial y}\right]+\alpha\frac{\omega}{k}P_k-\beta\rho\omega^2. \quad (5)$$

The turbulent viscosity (μ_T) expressed as:

$$\mu_T = p\frac{k}{\omega}, \quad (6)$$

where F_1 is the blending function which takes the value between 0 and 1, ρ is the density of air, and u, v, and w are the corresponding velocities of air in a bladeless fan in x, y, and z Cartesian coordinates, respectively [19].

2.4.4. Equation of Motion

$$m\ddot{x}+c\dot{x}+kx=F_l(t), \quad (7)$$

where c is a small damping coefficient and

$$F_l(t)=\frac{1}{2}\rho AU^2C_l(t). \quad (8)$$

2.5. Numerical Validation

The numerically predicted values of normalized displacement against wind velocity are compared with the results from the literature [20]. The boundary conditions for the present simulation are as obtained from the literature. The length and diameter of the bluff body are considered to be 120 mm and 32 mm, respectively.

The inlet velocity was varied between 0.5 m/s and 4 m/s. The number of grid elements is maintained as 0.7 million for numerical validation. Figure 6 shows the variation of Y_{max}/D against the wind velocities, and the predicted results closely match the literature results in [20]. The maximum deviation is less than 10% for an inlet velocity of 3 m/s. It should be noted that the present numerical simulations do not consider the damping contributions from structural, electrical, and drag related sources.

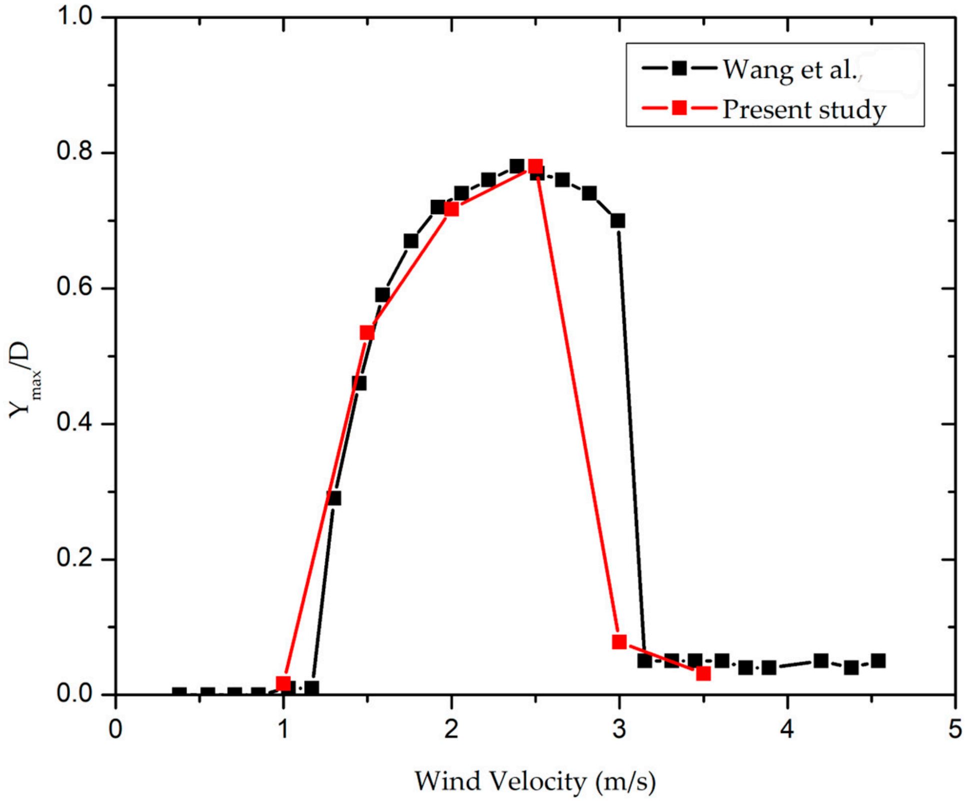

Figure 6. Comparison of maximum amplitude against the wind velocity with the small damping present in the study versus Wang et al. [20] with the fitting of the small damping coefficient.

3. Results and Discussion

The present study numerically investigates the influence of a passive jet control system on the performance of a VIV energy harvester. The baseline configuration consists of a circular cross-sectional profile, while the modified cases incorporate holes/perforations with a single inlet and symmetrical dual outlets at varying outlet angles, namely 30°, 60°, 90°, and 120°. The incoming wind velocities are varied between 1 m/s and 8 m/s with intervals of 1 m/s to understand the dynamic behavior of the passive jet system with various inflow conditions. The configuration without any passive jet system acts as a benchmark case for comparison, and passive jets are introduced to alter the flow dynamics around the bluff body by introducing a secondary flow through inlet and outlet holes. These additional secondary flows support earlier or delay inflow separation, and enhance the performance of VIV.

Additionally, in this PJCS configuration, the oscillation amplitude was measured using peak-to-peak values. Although some numerically predicted results exhibited transient chaotic behavior, a more detailed analysis is required to completely understand the transient chaotic dynamics and their implications. However, the present work primarily focuses on the impact of the PJCS on the system's performance, and therefore, the peak-to-peak response was deemed sufficient for the scope of this study.

In the base configuration, the vortex shedding is completely governed by the bluff body shape and incoming wind velocity. At lower wind velocities (up to 3 m/s), the vortices in the wake are weak, resulting in a limited energy transfer to the structure, and the oscillation amplitude increased from 5 mm to 40 mm at 2 m/s. As the wind velocity increases, the vortex shedding becomes more pronounced, with stronger and more coherent vortices forming in the wake. At a wind velocity of 5 m/s, the oscillation amplitude reaches its peak value of 51 mm, as shown in Figure 7. Interestingly, the frequency-locking phenomenon is not preserved for the whole interval of the enhanced response, as expected from the previous results [20]. This fact can be explained by the related Fourier power spectra (Figure 8). For a wind velocity of U = 3 and 4 m/s (Figure 8a,b), one can see the single peak associated with the natural frequency of the beam–bluff body structure. However, for higher wind velocities (U = 7 and 8 m/s—Figure 8c,d), the character of the solution is changed to two peaks with a leading peak of higher frequency, which is approximately [2–2.5] times higher. As the solution seems to be of quasi-periodic nature, the ratio of the leading frequency to the natural frequency is not a rational number. We claim that the large response amplitude is preserved across growing wind velocities because of the presence of bifurcations in the bluff body motion.

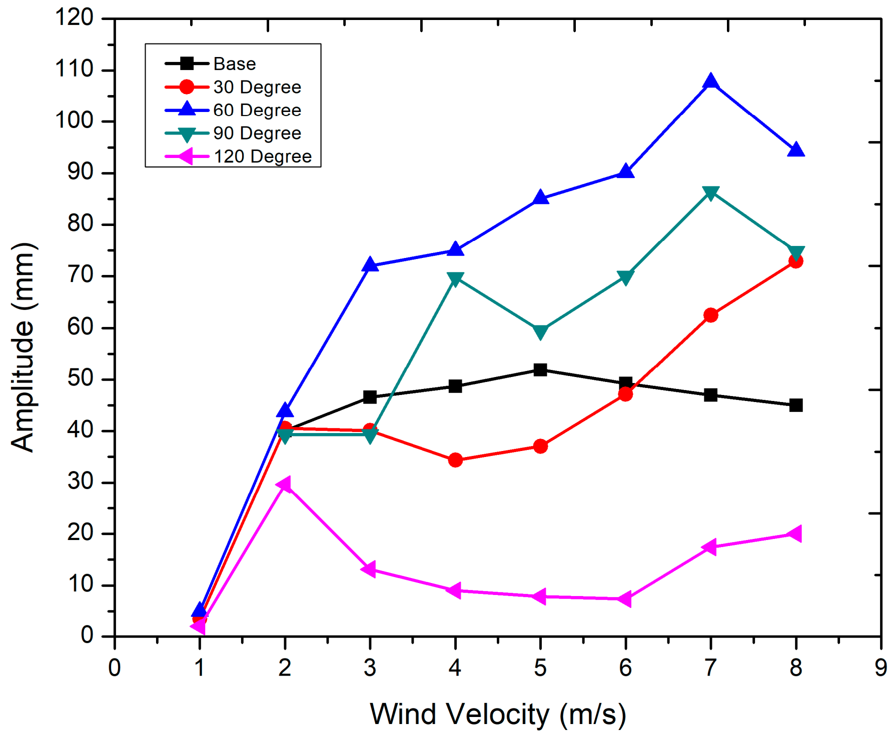

Figure 7. Cylinder amplitude vs. wind velocity of the base and passive jet configuration. Here, the damping coefficient c was neglected. The amplitudes are estimated from the half of the difference between the maximum and minimum values.

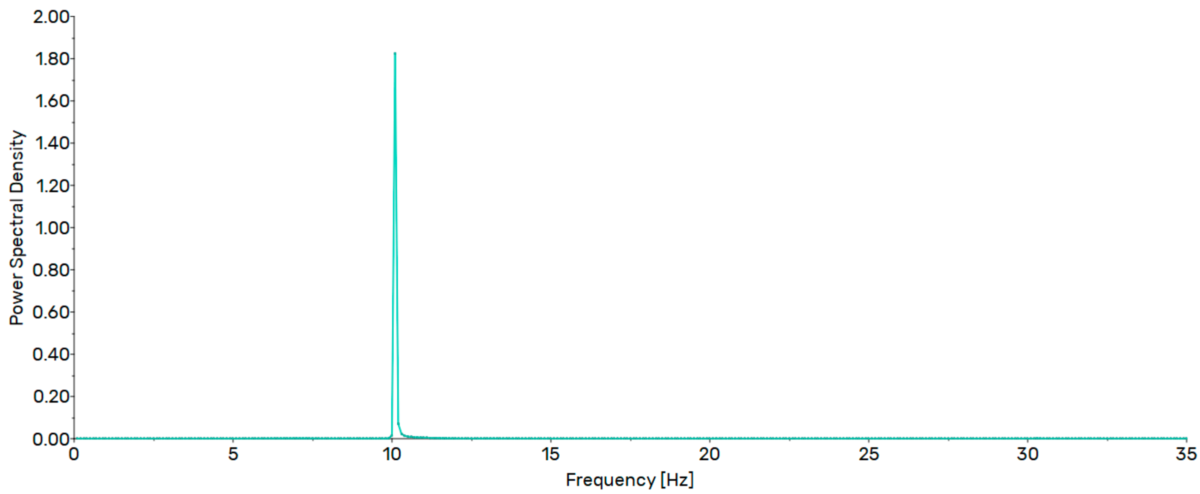

(**a**) U = 3 m/s

Figure 8. *Cont.*

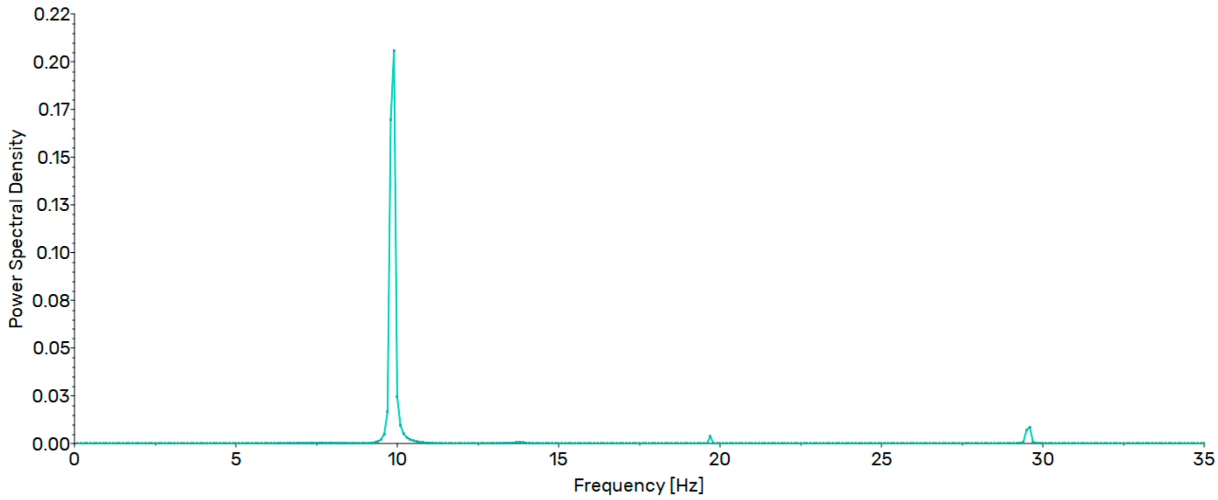

(**b**) U = 4 m/s

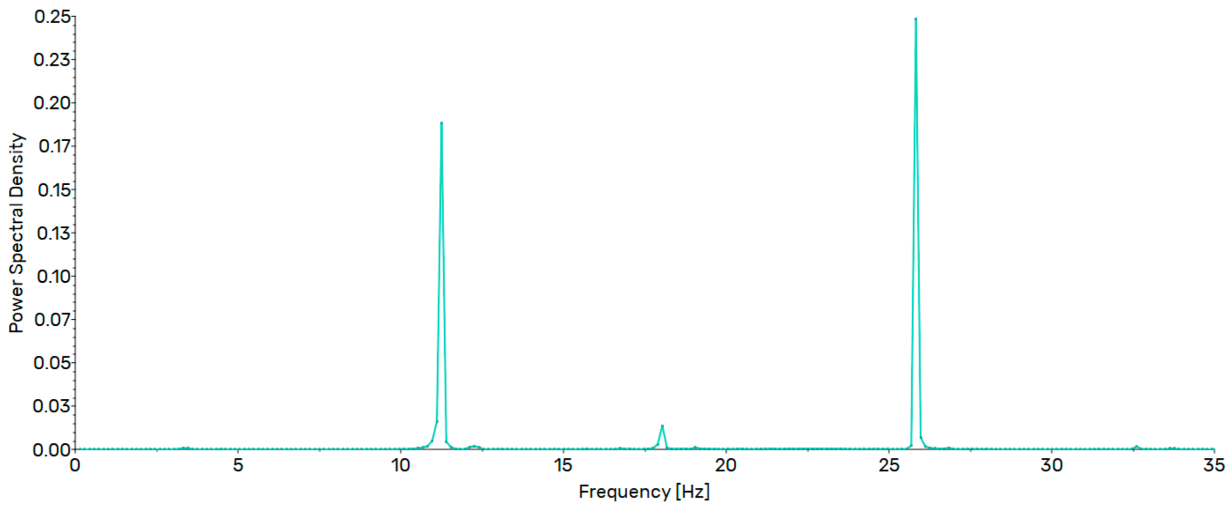

(**c**) U = 7 m/s

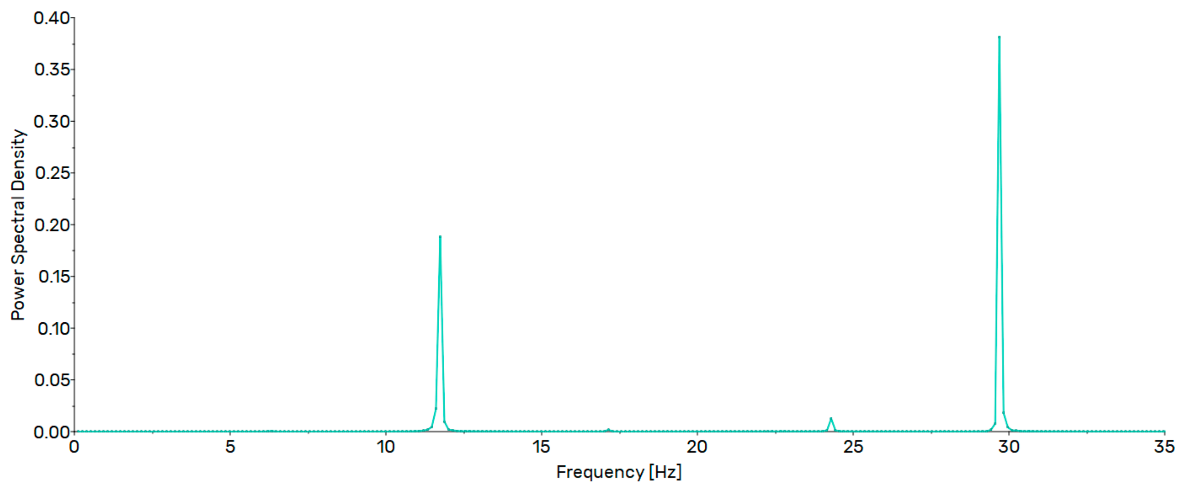

(**d**) U = 8 m/s

Figure 8. Power Spectral Density against the frequency plot of the bluff body displacement time series for the bluff body without channels. The various inlet cases (**a**–**d**) correspond to the different air inlet velocities U = 3, 4, 7, 8 m/s, respectively.

Note that beyond 5 m/s, the amplitude begins to decrease, due to the onset of a complex or non-periodic/chaotic vortex shedding and an earlier flow detachment from the bluff body surface. This behavior highlights the role of boundary layer separation and vortex coherence in influencing the VIV response. At lower velocities, a weak vortex shedding leads to limited oscillation amplitudes, while at higher velocities, a premature boundary layer separation causes chaotic vortex dynamics, reducing flow stability. The vorticity contours in Figure 9a–d confirm that as the inlet velocity increases, the vortex formation becomes increasingly unstable, leading to a diminished energy transfer and increased aerodynamic damping. These observations underscore the significance of maintaining vortex coherence and delaying boundary layer separation to optimize performance.

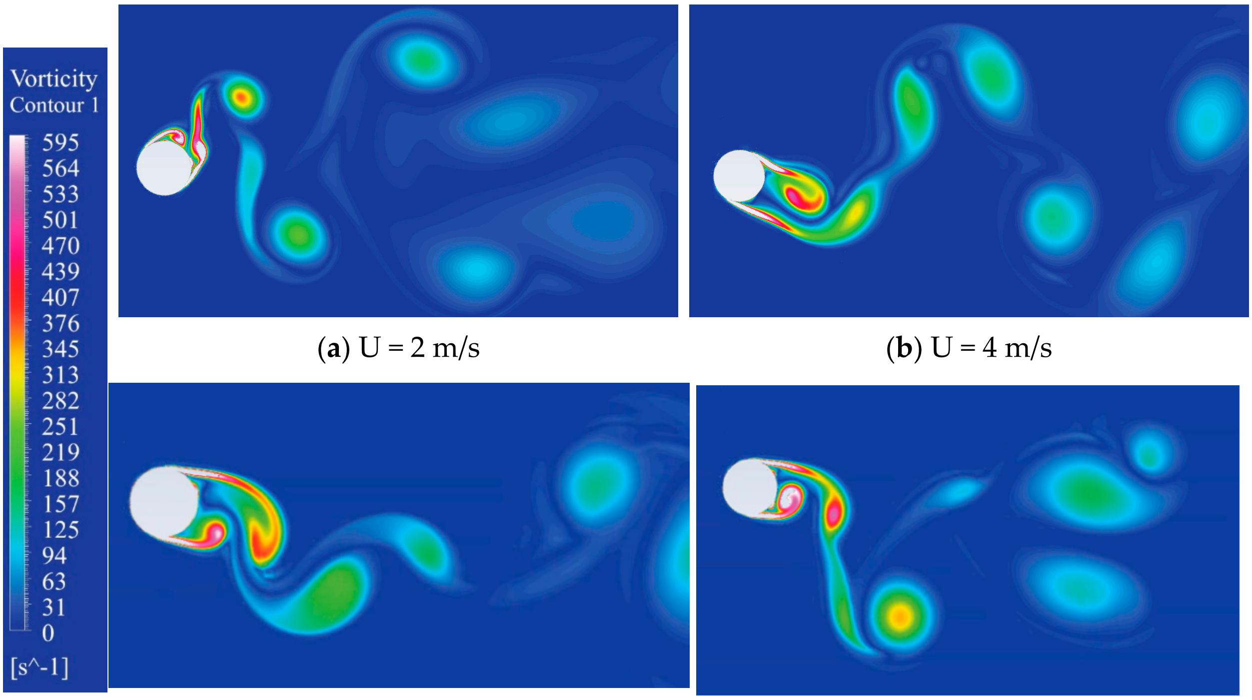

(**a**) U = 2 m/s (**b**) U = 4 m/s (**c**) U = 6 m/s (**d**) U = 8 m/s

Figure 9. (**a**–**d**) Vorticity contour of the baseline configuration.

In the Passive Jet Control System (PJCS) configuration with an outlet angle of 30 degrees, the behavior is similar to the baseline configuration at low wind velocities up to 3 m/s, with an oscillation amplitude of 40.1 mm. However, as the wind velocity increases to 6 m/s, the oscillation amplitude decreases significantly, indicating a decline in the VIV performance, as shown in Figure 7. This reduction is primarily due to the influence of passive jets on the boundary layer dynamics. The passive jets, nearly aligned with the main flow, stabilize the boundary layer and reduce the separation angle, weakening the strength and coherence of the vortices. This disruption in the natural vortex shedding process results in a decrease in oscillation amplitude, as supported by the vorticity contours in Figure 10a–e, whereas at higher velocities at 7 m/s and above, as shown in Figure 10f, the passive jets introduce additional momentum into the wake, altering the flow dynamics. The improvements in oscillation amplitude at these higher velocities are more likely due to momentum effects rather than the conventional VIV phenomenon. These findings highlight that passive jets aligned with the main flow are effective in reducing oscillations, but may not maximize energy transfer through VIV.

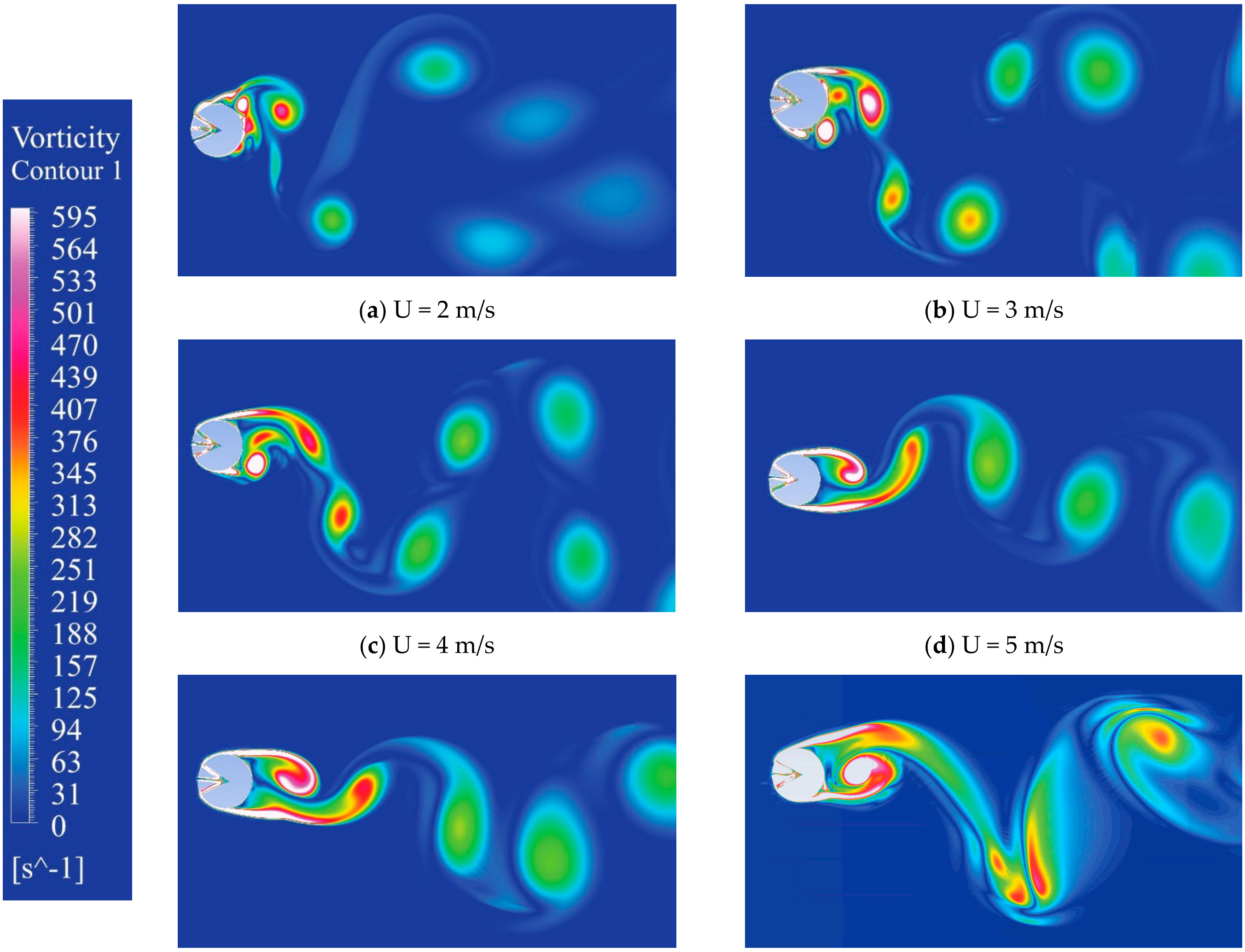

(**a**) U = 2 m/s (**b**) U = 3 m/s

(**c**) U = 4 m/s (**d**) U = 5 m/s

(**e**) U = 6 m/s (**f**) U = 7 m/s

Figure 10. (**a**–**f**) Vorticity contour of PJCS with the 30° outlet angle.

When the outlet angle was increased to 60 degrees, the secondary jets were directed diagonally into the incoming flow. The outlet angle of 60° demonstrated a more significant improvement in performance than the baseline configuration for all incoming wind velocities considered in this study. The maximum oscillation amplitude is recorded as 105 mm, which is a 94.4% increase compared to the baseline configuration maximum of 54 mm at 5 m/s. This performance improvement is attributed to the interaction between the passive jets and the natural vortex shedding flow. The diagonal alignment of the jets enhances vortex coherence by reinforcing the strength and stability of the shedding vortices. This alignment delays boundary layer separation and widens the lock-in region, and allows for an efficient energy transfer from the flow to the structure. However, further increasing the velocity to 8 m/s reduces the amplitude to 95 mm, a 9.5% drop, possibly due to vortex instability or the increased damping effects at higher velocities, as shown in Figure 7. These secondary jets align with the natural vortex shedding flow and enhance the strength and stability of the vortices, as shown in Figure 11a–f. This alignment delays boundary layer separation and optimizes the interaction with vortex dynamics, broadening the lock-in region and maximizing energy transfer from the flow to the structure. This configuration substantiates the potential of passive jets to modulate vortex dynamics effectively when optimally aligned.

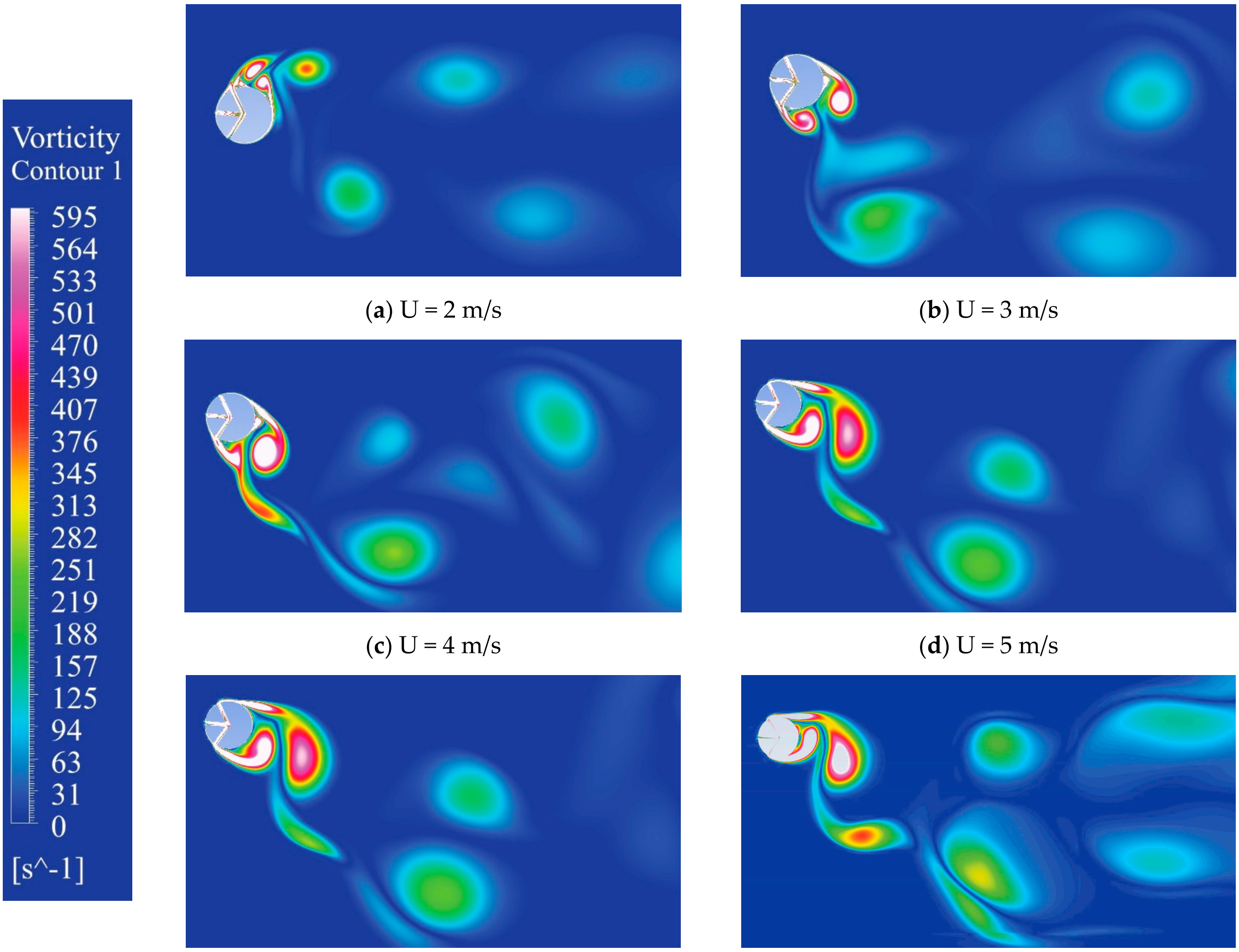

(**a**) U = 2 m/s (**b**) U = 3 m/s

(**c**) U = 4 m/s (**d**) U = 5 m/s

(**e**) U = 6 m/s (**f**) U = 7 m/s

Figure 11. (**a**–**f**) Vorticity contour of PJCS with the 60° outlet angle.

When the outlet angle is maintained at 90 degrees, the secondary jets are directed perpendicular to the main flow. At lower velocities, up to 3 m/s, the secondary jets lack sufficient momentum to significantly influence the main flow, particularly in controlling the boundary layer angle and delaying separation. As a result, VIV performance is reduced compared to the baseline configuration, as shown in Figure 7. However, at higher velocities, the secondary jets interact more effectively with the wake, enhancing the stability and strength of the vortices. This improved alignment results in a maximum oscillation amplitude of 86 mm at 7 m/s, representing nearly a 60% improvement compared to the baseline performance, and also extends the lock-in region, leading to the better VIV performance as shown in Figure 12a–e. Beyond 7 m/s, the performance declines due to vortex instability, increased aerodynamic damping, and a premature boundary layer separation, which reduce the coherence of vortex shedding and the efficiency of energy transfer, as shown in Figure 12f. These findings indicate that the 90° configuration is effective within a specific velocity range, providing a broader lock-in region but a reduced efficiency at higher velocities.

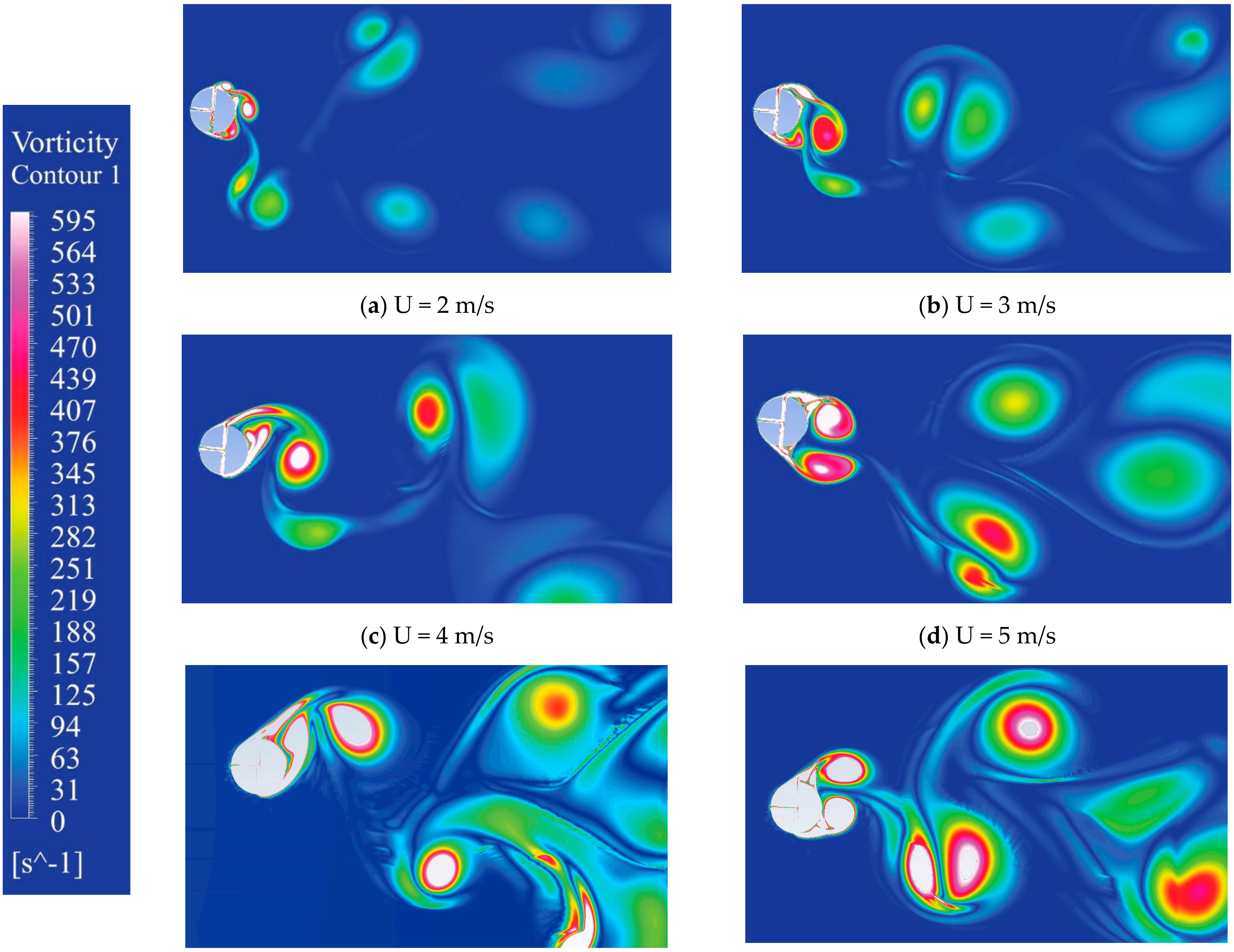

(**a**) U = 2 m/s (**b**) U = 3 m/s

(**c**) U = 4 m/s (**d**) U = 5 m/s

(**e**) U = 6 m/s (**f**) U = 7 m/s

Figure 12. (**a**–**f**) Vorticity contour of PJCS with the 90° outlet angle.

On the other hand, the outlet angle of 120° underperforms across all the wind velocities ranging between 1 m/s and 8 m/s. The 120-degree alignment disrupts the natural vortex shedding mechanism, and the secondary jets are directed towards primary vortices, causing interference with their formation and weakening them. This alignment accelerates boundary layer separation, reduces vortex coherence, and disrupts the synchronization of the shedding process. As a result, the energy transfer between the flow and the structure becomes inefficient, leading to poor VIV performance. The maximum amplitude recorded is 29 mm at 2 m/s, and as the velocity increases, the chaotic and unsynchronized vortex dynamics further diminish the resonance between the shedding frequency and the structure's natural frequency. This behavior is evident in Figure 13a–f where the vorticity contours show erratic and unstable vortex patterns. The 120° configuration, therefore, highlights the importance of aligning passive jets to support rather than interfere with natural vortex dynamics for effective flow control and energy transfer.

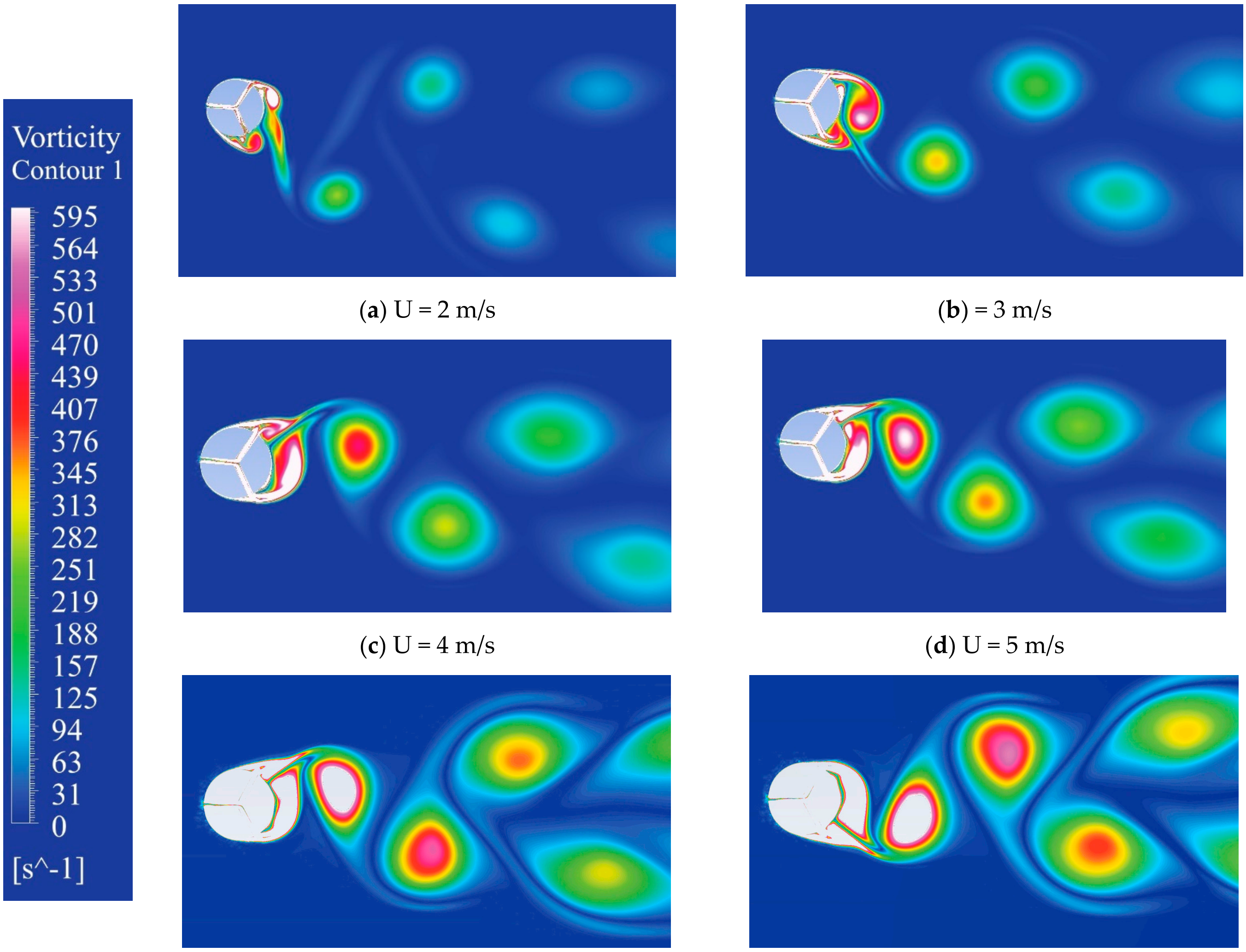

(**a**) U = 2 m/s (**b**) = 3 m/s

(**c**) U = 4 m/s (**d**) U = 5 m/s

(**e**) U = 6 m/s (**f**) U = 7 m/s

Figure 13. (**a**–**f**) Vorticity contour of PJCS with the 120° outlet angle.

Furthermore, the time history plot of the PJCS with the symmetrical dual outlet angles of 30°, 60°, 90°, and 120° is presented in Figure 14a–d for the inlet wind velocities ranging from 1 m/s to 8 m/s. The time history data is presented for the interval between 9 and 10 s where the numerical simulation has reached a steady state. The study revealed that at lower wind velocities, the energy available in the flow is insufficient to sustain strong vortex shedding, leading to periodic oscillations with low amplitude. The same behavior was observed across all the outlet angles. As the wind velocity increased to 3 m/s and above, a notable improvement in oscillation amplitude was observed, and the vortex shedding becomes more intense, resulting in higher amplitude oscillations, particularly for the 60° outlet angle, which optimally aligns with the flow conditions to enhance the lock-in region and amplify oscillations. The maximum amplitude was recorded for the 60° outlet angle at 5 m/s. At wind velocities above 6 m/s, the interaction between the flow and the bluff body became more complex, causing transient chaotic behavior for the 30° and 90° outlet angles. In contrast, the 60° and 120° outlet angles performed better by stabilizing the flow and maintaining periodic responses. However, the maximum oscillation amplitude decreased beyond this point, and the 120° angle exhibited a poorer response compared to the baseline configuration.

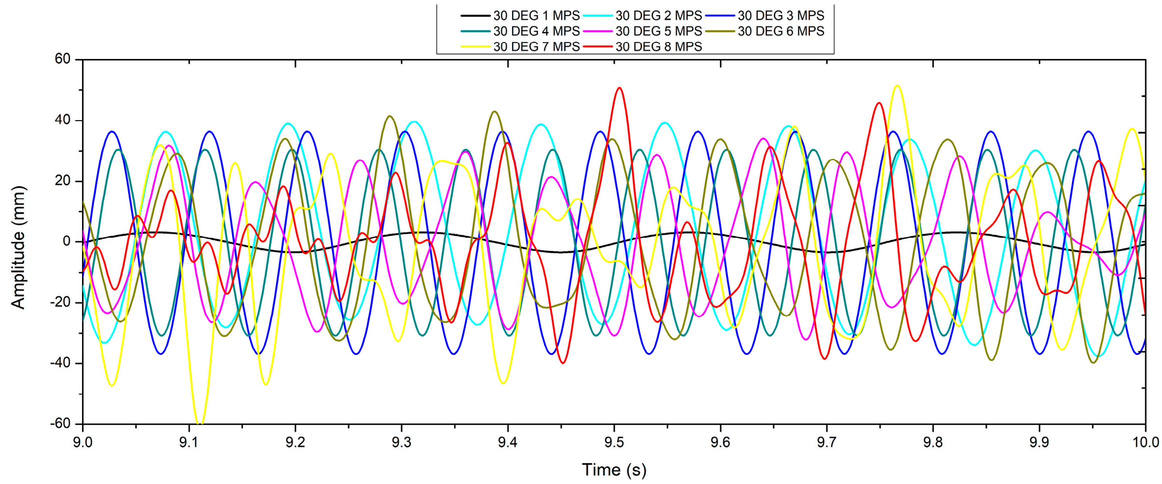

(**a**) 30 degrees—symmetrical dual outlet

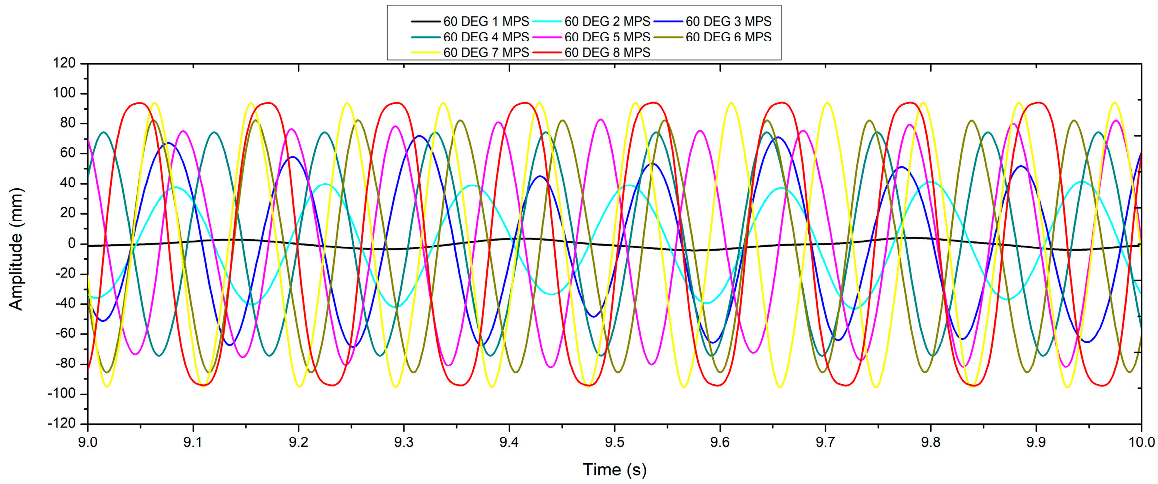

(**b**) 60 degrees—symmetrical dual outlet

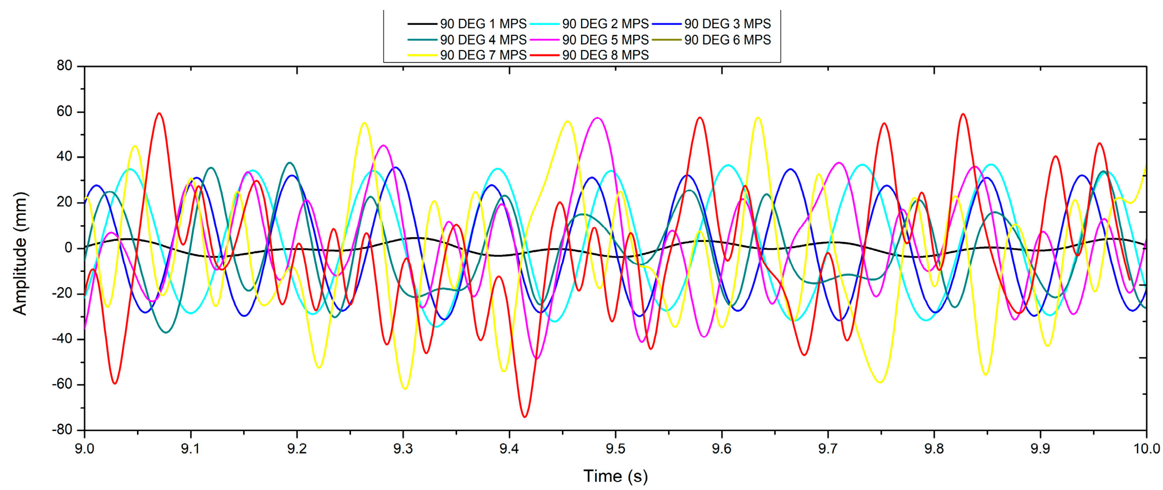

(**c**) 90 degrees—symmetrical dual outlet

Figure 14. *Cont.*

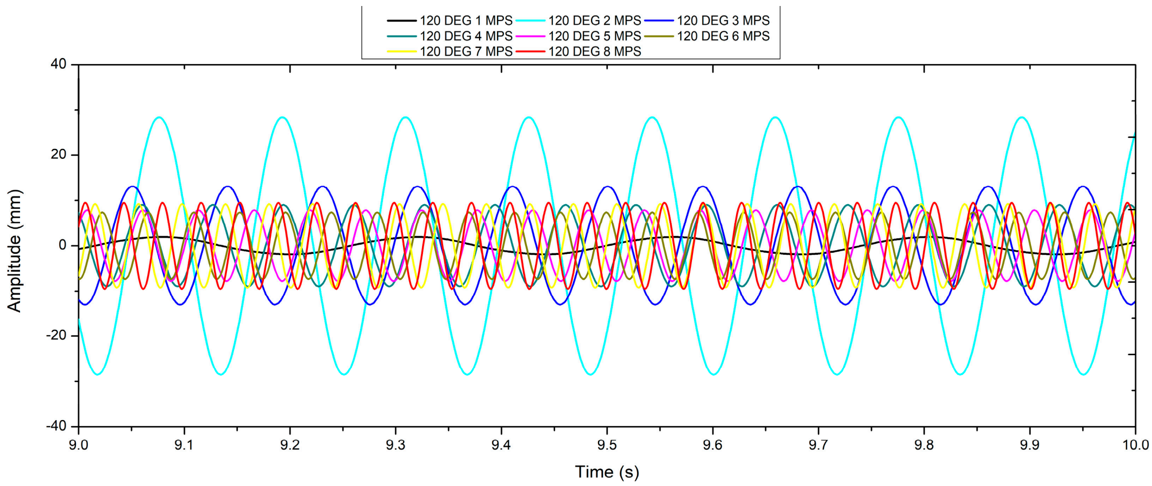

(**d**) 120 degrees—symmetrical dual outlet

Figure 14. (**a**–**d**) Time history of the bluff body motion of the varying symmetrical dual outlet angles with the different inlet velocities.

Based on the corresponding time histories of the bluff bodies presented in Figure 14, the amplitudes in Figure 7 were estimated. Most of the responses are periodic but Figure 14c (90 degree channels) shows presumably aperiodic responses for 4–8 m/s. The aperiodic amplitude response observed in the 90° outlet configuration for the velocities exceeding 4 m/s may be due to a complex interaction of the passive jet system with the conventional VIV shedding phenomenon. As the flow velocity increases, shear layer instabilities develop at the outlet edges, leading to irregular vortex formation and shedding, which in turn disrupts the periodic nature of the amplitude response. Additionally, the abrupt redirection of flow due to the 90° outlet angle alters recirculation zones and promotes premature flow separation, which contributes to transient pressure variations and further enhances unsteady behavior. At higher velocities, even minor perturbations break the expected flow symmetry between the dual outlets, resulting in asymmetric flow distribution and chaotic fluctuations. However, this aperiodic behavior is mostly absent in the 30°, 60°, and 120° outlet configurations. In these cases, the smoother flow redirection reduces recirculation effects and vortex-induced instabilities, allowing for a more stable and periodic amplitude response. The gradual deflection in the 30° and 60° outlet angle minimizes the abrupt shear layer separation, while the wider 120° outlet angle interacts with the primary vortices and disrupts it. These factors contribute to a more predictable flow pattern with fewer chaotic fluctuations. The findings of the present study provide a deeper understanding of vortex shedding behavior and its frequency under varying outlet angles and configurations. The incorporation of perforations in the bluff body, combined with single inlet and multiple outlet configurations, demonstrates significant potential for controlling the mass of the bluff body, and this would ideally help in the control and optimization of the system resonance frequency. By adjusting the outlet angles, the study reveals how flow characteristics and oscillatory responses can be tailored to achieve a wider lock-in region across different flow conditions.

4. Conclusions

A two-dimensional numerical investigation was carried out to understand the dynamic response of the VIV energy harvester with the passive jet control system. Four different outlet configurations, namely 30°, 60°, 90°, and 120° were tested and compared against the base configuration—a circular cross section profile. Note that real 3D shapes of the bluff bodies cannot be simply reduced to a 2D case, but our preliminary approximate 2D studies show the tendencies that could be also present in 3D cases. The bifurcation phenomena noticed in the dynamical responses of the bluff body motion also need to be further highlighted by comparative studies of approximate models [21].

Based on the present numerical investigation and the corresponding results and discussions from the present study, the following conclusions may be summarized:

(a) The symmetrical dual outlet channel with 30-degree inclination exhibits similar and reduced performance compared to the baseline configuration at low and intermediate wind velocities, respectively. However, at higher wind velocities, i.e., 6 m/s and above, it showed a significant improvement of nearly 10% in oscillation amplitude. The 30-degree configuration effectively stabilizes vortices at higher wind velocities but proves inefficient at lower velocity ranges.

(b) An outlet angle of 60 degrees significantly enhances performance across all tested wind velocities, with a maximum oscillation amplitude of 105 mm at 5 m/s—94.4% higher than the baseline. While amplitude decreases slightly at higher velocities (e.g., 95 mm at 8 m/s), the configuration effectively aligns secondary jets with vortex shedding, delaying a boundary layer separation and optimizing vortex dynamics to maximize energy transfer.

(c) With a 90-degree outlet angle, secondary jets initially show limited influence at low velocities (up to 3 m/s), resulting in reduced performance compared to the baseline. At higher velocities (up to 7 m/s), their interaction with the wake enhances vortex stability and strength, achieving a maximum oscillation amplitude of 86 mm, a 60% improvement over the baseline. However, beyond 7 m/s, its performance declines due to vortex instability, increased damping, and the early boundary layer separation.

(d) The 120-degree outlet angle demonstrated a smaller peak-to-peak shedding distance and a reduced oscillation amplitude, which suggests that although the vortex shedding frequency has increased, it is no longer synchronized with the bluff body's natural frequency. This mismatch, along with potential vortex weakening and higher damping effects, results in a less efficient energy transfer and thus smaller oscillation amplitudes. The main results, presented in Figure 7, indicate that the energy harvesting with the piezoelectric converted on the elastic suspension can be more effective for the canals with 60°, which is consistent with the recent finding in [14].

(e) By adding perforations to the bluff body and experimenting with single-inlet and multiple-outlet configurations, the mass of the bluff body can be controlled to optimize its resonance frequency. This approach will be helpful in designing the bluff body for VIV energy harvesting. These results offer practical relevance by enabling the design of passive jet control systems adaptable to various bluff body geometries and flow conditions.

Author Contributions: Conceptualization, G.L. and D.R.; methodology, D.R.; software, D.R.; validation, D.R.; formal analysis, M.W. and M.F.; investigation, D.R.; resources, G.L. and M.F.; data curation, M.W.; writing—original draft preparation, D.R., M.W., M.F. and G.L.; writing—review and editing, G.L. and D.R.; visualization, M.W. and M.F.; supervision, G.L.; project administration, G.L.; funding acquisition, G.L. All authors have read and agreed to the published version of the manuscript.

Funding: This research was funded by National Science Centre, Poland under the project SHENG-2, No. 2021/40/Q/ST8/00362.

Data Availability Statement: The data presented in this study are available upon request from the corresponding author.

Acknowledgments: The authors thank A.M. Giri from Lublin University of Technology for helpful discussions.

Conflicts of Interest: The authors declare no conflicts of interest. The funders had no role in the design of the study; in the collection, analyses, or interpretation of the data; in the writing of the manuscript; or in the decision to publish the results.

Abbreviations

BB	Bluff Body
CFD	Computational Fluid Dynamics
Cr	Roughness Coefficient
D	Diameter of bluff body
L	Length of bluff body
PTC	Passive Turbulence Control
t	Time
ts	Time step size
U	Wind Velocity
VIV	Vortex Induced Vibration
Y	Oscillation Amplitude
Y_{max}	Maximum Oscillation Amplitude

References

1. Elijah, O.; Rahman, T.A.; Orikumhi, I.; Leow, C.Y.; Hindia, M.N. An overview of internet of things (iot) and data analytics in agriculture: Benefits and challenges. *IEEE Internet Things J.* **2018**, *5*, 3758–3773. [CrossRef]
2. Mazunga, F.; Nechibvute, A. Ultra-low power techniques in energy harvesting wireless sensor networks: Recent advances and issues. *Sci. Afr.* **2021**, *11*, e00720. [CrossRef]
3. Garcia-Sanchez, A.J.; Garcia-Sanchez, F.; Garcia-Haro, J. Wireless sensor network deployment for integrating video-surveillance and data-monitoring in precision agriculture over distributed crops. *Comput. Electron. Agric.* **2011**, *75*, 288–303. [CrossRef]
4. Ijaz, H.; Ma, B.F. Unsteady vortex flows around a hemisphere—Cylinder body with turbulent separation. *Phys. Fluids* **2022**, *34*, 077105. [CrossRef]
5. Duan, G.; Laima, S.; Chen, W.; Li, H. Effects of leading-edge separation on the vortex shedding and aerodynamic characteristics of an elongated bluff body. *J. Wind Eng. Ind. Aerodyn.* **2020**, *206*, 104356. [CrossRef]
6. Mehdipour, I.; Madaro, F.; Rizzi, F.; De Vittorio, M. Comprehensive experimental study on bluff body shapes for vortex-induced vibration piezoelectric energy harvesting mechanisms. *Energy Convers. Manag. X* **2022**, *13*, 100174. [CrossRef]
7. Wang, X.; Chen, J.; Zhou, B.; Li, Y.; Xiang, Q. Experimental investigation of flow past a confined bluff body: Effects of body shape, blockage ratio and Reynolds number. *Ocean Eng.* **2021**, *220*, 108412. [CrossRef]
8. Zheng, M.; Han, D.; Gao, S.; Wang, J. Numerical investigation of bluff body for vortex induced vibration energy harvesting. *Ocean Eng.* **2020**, *213*, 107624. [CrossRef]
9. Owen, J.C.; Bearman, P.W.; Szewczyk, A.A. Passive control of viv with drag reduction. *J. Fluids Struct.* **2001**, *15*, 597–605. [CrossRef]
10. Chen, W.L.; Chen, G.B.; Xu, F.; Huang, Y.W.; Gao, D.L.; Li, H. Suppression of vortex-induced vibration of a circular cylinder by a passive-jet flow control. *J. Wind Eng. Ind. Aerodyn.* **2020**, *199*, 104119. [CrossRef]
11. Chen, G.; Chen, W.; Min, X.; Gao, D. A coupled model for vortex induced vibration of a circular cylinder with and without passive-jet flow control. *J. Fluids Struct.* **2022**, *110*, 103541. [CrossRef]
12. Chen, G.; Chen, W.L.; Chen, C.; Gao, D.; Meng, H.; Kim, K.C. Experimental and coupled model investigation of an active jet for suppressing vortex-induced vibration of a box girder. *J. Fluids Struct.* **2024**, *127*, 104119. [CrossRef]
13. Youssef, M.; el Moctar, O.; el Sheshtawy, H.; Tödter, S.; Schellin, T.E. Passive flow control of vortex-induced vibrations of a low mass ratio circular cylinder oscillating in two degrees-of-freedom. *Ocean Eng.* **2022**, *254*, 111366. [CrossRef]
14. Wang, J.; Han, C.; Yurchenko, D.; Zhou, Y.; Meng, X.; Zhang, W. Energy concentration pipe based on passive jet control for enhancing flow induced vibration energy harvesting. *Energy Convers. Manag.* **2024**, *319*, 118948. [CrossRef]
15. Wu, J.; Xu, P.; Li, L.; Li, Z.; Qi, H.; Wang, C.; Zhang, Y.; Xie, Y.; Tan, D. Multiphase dynamic interfaces and abrasive transport dynamics for abrasive flow machining in shear thickening transition states. *Powder Technol.* **2024**, *446*, 120150. [CrossRef]
16. Wang, C.; Li, Z.; Xu, P.; Hou, Y.; Tan, D.; Li, L. Collision modeling approach and transient response mechanism of ring-ribbed cylindric shells for underwater vehicles. *Appl. Math. Model.* **2025**, *141*, 115923. [CrossRef]

17. Wu, J.; Shen, M.; Jiang, L. Role of synthetic jet control in energy harvesting capability of a semi-active flapping airfoil. *Energy* **2020**, *208*, 118389. [CrossRef]
18. Gu, Y.; Huang, Z.; Zheng, C.; Chen, Z. The effects of pulsed blowing jets on power gain of vortex-induced vibrations of a circular cylinder. *Phys. Fluids* **2023**, *35*, 045134. [CrossRef]
19. Boussouar, G.; Rostane, B.; Aliane, K.; Ravi, D.; Gęca, M.J.; Gola, A. Study of the Thermal Performance of Solar Air Collectors with and without Perforated Baffles. *Energies* **2024**, *17*, 3812. [CrossRef]
20. Wang, J.; Zhang, Y.; Liu, M.; Hu, G. Etching metasurfaces on bluff bodies for vortex-induced vibration energy harvesting. *Int. J. Mech. Sci.* **2023**, *242*, 108016. [CrossRef]
21. Li, Z.; Zhang, H.; Litak, G.; Zhou, S. Periodic solutions and frequency lock-in of vortex-induced vibration energy harvesters with nonlinear stiffness. *J. Sound Vib.* **2024**, *568*, 17952. [CrossRef]